

Machine learning-driven prediction of mechanical properties for 3D printed concrete

Junzan Li¹, Linhui Wu², Zihan Huang¹, Yin Xu³ and Kaihua Liu^{*1}

¹School of Civil and Transportation Engineering, Guangdong University of Technology, Guangzhou, 510006, China

²School of Computer Science and Technology, Guangdong University of Technology, Guangzhou, 510006, China

³China Tunnel Construction Group Co., Ltd Guangdong, Guangzhou, 510801, China

(Received June 18, 2024, Revised June 19, 2024, Accepted July 26, 2024)

Abstract. Mechanical performance is crucial for 3D printed concrete, as it directly influences the structural load-bearing capacity and safety. However, the inherent complexities and variability of the material pose significant challenges in achieving accurate predictions of its mechanical performance. This study introduces a novel approach to predict the compressive strength (CS) and flexural strength (FS) of 3D printed concrete using machine learning (ML) methods. A comprehensive database containing 254 CS tests and 210 FS tests was established to train four ML models: artificial neural networks, random forest, extreme gradient boosting, and categorical boosting algorithms (CatBoost). The CatBoost model demonstrated superior performance, with R^2 values of 0.929 for CS and 0.967 for FS on the test set. To provide insights into the model's predictions, partial dependence plots and Shapley Additive Explanations were employed, revealing that the water-to-binder ratio ($n(W/B)$) and the content of ordinary Portland cement are critical factors influencing CS, while $n(W/B)$ and the content of ground granulated blast furnace slag significantly affect FS. This innovative ML-driven approach offers a robust framework for accurately predicting the mechanical properties of 3D printed concrete, thereby enhancing its application in structural engineering.

Keywords: 3D printed concrete; compressive strength; flexural strength; machine learning; partial dependence plots; SHAP

1. Introduction

As an efficient means to achieve digitalization, intelligence, and automation in construction, 3D printing construction technology is an important method for transforming and upgrading the traditional construction industry (Dilawar *et al.* 2023). 3D printed concrete (3DPC) acts as a printing ink. In contrast to conventional concrete, 3DPC is built by stacking layers, making it suitable for creating complex geometries and unique architectural designs (Qaidi *et al.* 2022).

Ensuring robust mechanical performance is essential for the practical application of 3DPC in construction, as any compromise in strength can lead to structural failures and safety hazards (Liu *et al.* 2023). Unlike traditional cast concrete, 3DPC involves layer-by-layer deposition, introducing anisotropy and heterogeneity within the printed structure. While mechanical performance is crucial for the safe and effective utilization of 3DPC in construction, accurately predicting its strength remains a significant challenge.

Testing the mechanical properties of 3DPC using test methods requires the preparation of many specimens and specialized equipment, resulting in high costs and being

time-consuming (Shishegaran *et al.* 2021). Trial and error, as well as optimization, further increase the time and expenses, limiting the efficiency of evaluating 3DPC performance in real-world applications (Young *et al.* 2019).

In recent years, machine learning (ML) has been widely used to solve problems such as classification, regression, and clustering because it can learn the rules and patterns of data through computers in massive datasets and mine potential information from them. In contrast to traditional empirical methods, ML is data-driven and can fully account for the nonlinear relationship between the independent and dependent variables. Additionally, ML can be applied to complex problems like solving partial differential equations (Anitescu *et al.* 2019, Goswami *et al.* 2020, Samaniego *et al.* 2020), offering efficient and accurate approximations. ML methods have started to be utilized in research within the field of civil engineering (Wang *et al.* 2023). Nguyen *et al.* (2021) utilized the support vector machine (SVM), multilayer perceptron (MLP), gradient boosting regression (GBR), and extreme gradient boosting (XGBoost) to forecast the compressive and tensile strength of high-performance concrete. They found that the GBR and XGBoost models performed better than other models. Mohammed *et al.* (2021a) utilized linear, nonlinear regression, M5P-tree, and artificial neural network to predict the compression strength of concrete containing polymers. Gomaa *et al.* (2021) used the Random Forest to predict fly ash-based polymer concrete's CS and slump. Ahmed *et al.* (2021) confirmed the feasibility of using ML

*Corresponding author, Associate Professor
E-mail: kaihualiu@gdut.edu.cn

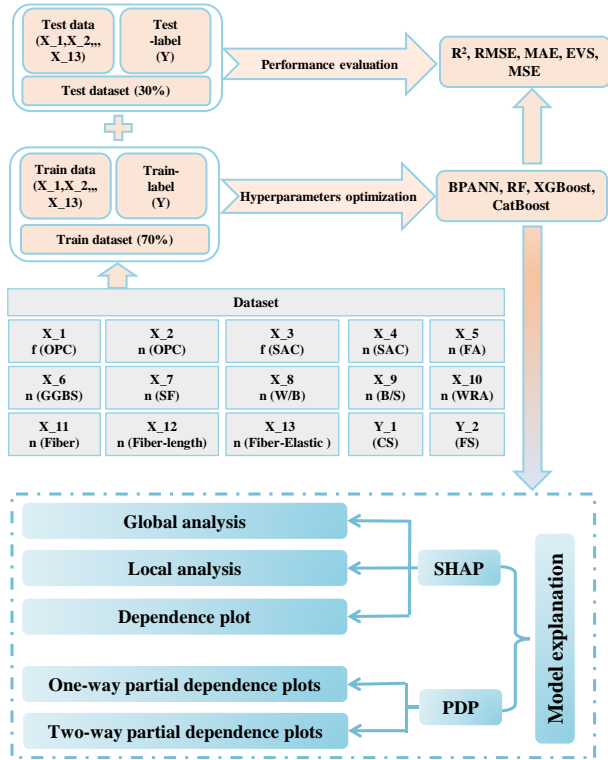


Fig. 1 Research framework

algorithms to forecast the CS of fly ash-based polymer concrete. Mohammed *et al.* (2021b) combined particle swarm optimization and an imperialist competitive algorithm with a pre-developed artificial neural network to improve the prediction of fly ash-modified concrete's CS. Zhang *et al.* (2022) used multiple nonlinear regression to establish a prediction model for the CS of lightweight high-strength concrete. Garg *et al.* (2022) proposed surrogate models to predict the CS of concrete containing nano-silica, based on SVM and Gaussian Process Regression techniques. Ahmed *et al.* (2022) developed ML models to predict the CS of high-strength concrete prepared with metakaolin. Ali *et al.* (2023) used the Gaussian process regression model, decision tree model, SVM, and XGBoost model to forecast the flexural and tensile strength of 3DPC. Their study revealed that the SVM model outperformed the other models. Piro *et al.* (2023) employed an artificial neural network model to effectively predict the CS of concrete incorporating steel slag aggregate, identifying curing time as the most significant influencing factor. Choudhary *et al.* (2024) used the six ML models to forecast the CS of ternary geopolymer concrete and found that GBR performs better than all other algorithms.

Ensuring robust mechanical performance is crucial for the practical application of 3DPC in construction, as any compromise in strength can result in structural failures and safety hazards. Unlike traditional cast concrete, 3DPC involves layer-by-layer deposition, which introduces anisotropy and heterogeneity within the printed structure. These inherent characteristics present significant challenges in accurately predicting the mechanical strength of 3DPC. The motivation for this research arises from the need to address these predictive challenges to fully exploit the

benefits of 3DPC, such as faster construction times, reduced material waste, and enhanced design flexibility. This study aims to develop an intelligent model capable of accurately predicting the mechanical properties of 3DPC. The integration of advanced ML techniques with comprehensive data analysis may yield a robust predictive model to overcome the anisotropic and heterogeneous nature of 3DPC and address the unique mechanical performance challenges posed by 3DPC. The study outlined in Fig. 1 explains the overall approach taken. Initially, a test database of the mechanical properties of 3DPC was created. Subsequently, four ML algorithms were utilized to train and test this dataset independently, identifying the most effective models for predicting the compressive and flexural strength of 3DPC. Finally, the interpretability of the model was analyzed using SHapley Additive exPlanations (SHAP) and Partial dependence plots (PDPs) techniques to understand the significance of each input parameter and its impact on the outcomes.

2. Methodology

2.1 Back propagation artificial neural network

Back Propagation neural network (BPANN) is a supervised learning algorithm designed to minimize the discrepancy between the predicted output and the actual target value through iterative optimization of weights and biases (Rumelhart *et al.* 1986). This process begins with forward propagation, where input data passes through the network to produce an output. The algorithm then calculates the gradient of the error between the predicted and actual values using the chain rule of differentiation. During backpropagation, these gradients are employed to update the network's weights and biases, thereby incrementally improving performance. BPANN utilizes the gradient descent method, continuously adjusting the parameters to minimize the error function, typically measured by mean squared error. The model operates under the assumption that the error can be minimized to an acceptable range. BPANN is known for its applicability in both classification and regression problems, offering a robust learning mechanism that is relatively straightforward to implement and understand. This intuitive error correction process via backpropagation has established BPANN as a fundamental tool in neural network research and applications. The following equation denotes weight updates

$$W_{ij}^{(t+1)} = W_{ij}^{(t)} - \eta \frac{\partial E}{\partial W} \quad (1)$$

where $W_{ij}^{(t)}$ represents the weight of the connection i to j in the t iteration, η represents the learning rate, E represents the error function of the network, and $\frac{\partial E}{\partial W}$ represents the partial derivative of the error function relative to the weight.

2.2 Random forest

Random forest (RF) is an ensemble learning method that integrates multiple decision trees to build a more robust

Table 1 The statistical description of variables in the compress strength database

Variable	Unit	Average	Minimum	Median	Maximum	Standard deviation
f(OPC)	MPa	46.40	42.5	42.5	52.5	4.88
n(OPC)	%	0.78	0	0.8	1	0.19
f(SAC)	MPa	42.5	42.5	42.5	42.5	0
n(SAC)	%	0.39	0	0.6	0.6	0.26
n(FA)	%	0.11	0	0	0.75	0.16
n(GGBS)	%	0.05	0	0	0.3	0.10
n(SF)	%	0.06	0	0.05	0.27	0.06
n(W/B)	--	0.29	0.15	0.3	0.65	0.08
n(B/S)	--	1.09	0.1	1	4.5	0.63
n(WRA)	%	0.54	0	0.35	1	0.54
n(Fb-E)	GPa	44.71	3	40	200	49.59
n(Fb-L)	mm	8.40	3	6	16	3.26
n(Fb)	%	0.35	0	0	4	0.59
CS	MPa	64.21	11.1	54	189	31.52

Note: f(OPC) represents ordinary Portland cement strength grade, n(OPC) represents ordinary Portland cement content, f(SAC) represents sulfoaluminate cement strength grade, n(SAC) represents sulfoaluminate cement content, n(FA) represents fly ash content, n(GGBS) represents ground granulated blast furnace slag content, n(SF) represents silica fume content, n(W/B) represents water-binder ratio, n(B/S) represents binder-sand ratio, n(WRA) represents water-reducing admixture content, n(Fb) represents fiber content, n(Fb-L) represents the length of fiber, n(Fb-E) represents the elastic modulus of fiber, and CS represents the 28-day CS of 3DPC.

Table 2 The statistical description of variables in the FS database

Variable	Unit	Average	Minimum	Median	Maximum	Standard deviation
f(OPC)	MPa	46.78	42.5	42.5	52.5	4.96
n(OPC)	%	0	0.69	0.75	1	0.16
f(SAC)	MPa	42.5	42.5	42.5	42.5	0
n(SAC)	%	0.33	0	0.35	0.6	0.27
n(FA)	%	0.07	0	0	0.6	0.09
n(GGBS)	%	0.05	0	0	0.3	0.08
n(SF)	%	0.05	0	0.05	0.27	0.05
n(W/B)	--	0.15	0.2	0.3	0.65	0.07
n(B/S)	--	0.1	1	1	2.49	0.17
n(WRA)	%	0.48	0	0.3	1	0.46
n(Fb-E)	GPa	3	3.1	30	200	25.22
n(Fb-L)	mm	3	6	6	16	2.02
n(Fb)	%	0.17	0	0	4	0.28
FS	MPa	11.47	0.14	11.7	45	4.80

Note: FS represents the 28-day FS of 3DPC.

model for regression and classification tasks by averaging predictions or voting (Breiman 2001). Raw data is randomly sampled with replacement to create diverse training datasets through a process called bootstrap aggregating or bagging. Each decision tree is constructed on an independent subsample, enhancing generalizability and reducing overfitting. At each node of a decision tree, a random subset of features is selected for partitioning, introducing randomness, and decorrelating the trees. This random feature selection at each node ensures that each tree explores different feature interactions, increasing model

diversity. By averaging the predictions of individual trees (for regression) or taking a majority vote (for classification), RF effectively mitigates overfitting risks associated with single decision trees. RF is highly valued for its accuracy, flexibility, and ease of use. The prediction results of the RF model can be expressed as follows

$$H(x) = \frac{1}{K} \sum_{i=1}^K h_i(x, \theta_k) \quad (2)$$

where $H(x)$ represents the prediction result of the random forest, K represents the number of decision trees, h_i



Fig. 2 Data distribution for all variables

represents the prediction result of the i^{th} decision tree, θ_k represents the independently distributed random variable that determines the growth process of a decision tree.

2.3 Extreme gradient boosting regression

Extreme gradient boosting regression (XGBoost) is a gradient-boosting tree-based ML algorithm designed to

enhance model performance by iteratively constructing a series of decision trees and integrating their residuals (Chen *et al.* 2016). Building on the original gradient-boosted tree algorithm, XGBoost introduces the differentiability of regularization terms and splitting nodes. This allows the model to select the optimal splitting point at each step, thereby improving precision and efficiency. The algorithm effectively handles high-dimensional data and complex

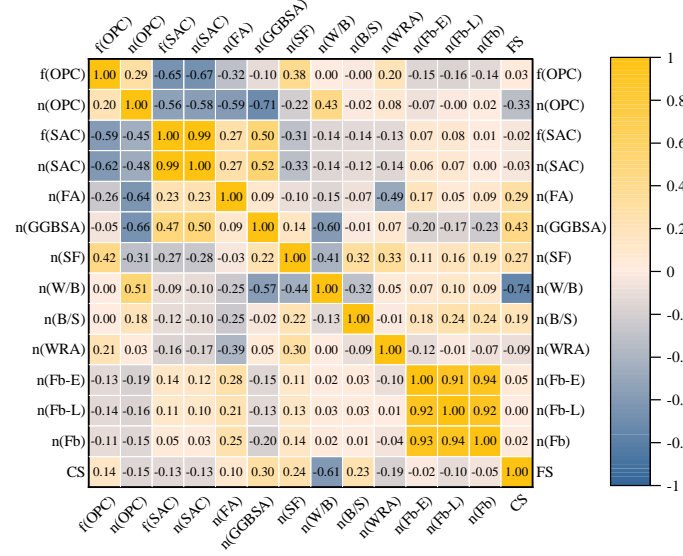


Fig. 3 Correlation analysis chart, the upper (lower) triangular matrix is the heatmap of FS (CS)

relationships, making it particularly suitable for large-scale and intricate datasets. By incorporating regularization, XGBoost prevents overfitting and ensures model robustness. The advanced features and scalability of XGBoost have established it as a powerful tool in predictive modeling and data analysis. The objective function can be expressed as follows

$$OBJ = \sum_{i=1}^N L(y_i, \hat{y}_i^{(t-1)} + f_t(x_i)) + \sum_{t=1}^T \Omega(f_t) \quad (3)$$

$$\Omega(f_t) = \gamma K + \frac{1}{2} \lambda \|\omega\|^2 \quad (4)$$

where L is the training loss, Ω is the regularization item, K is the number of leaf nodes, ω is the fraction of leaf nodes, γ and λ represent the coefficient to prevent overfitting.

2.4 Categorical boosting

Categorical Boosting (CatBoost) is a gradient-boosting tree-based ML algorithm that introduces an innovative technique called Ordered Boosting (Prokhorenkova *et al.* 2019). This technique constructs each tree based on the structure of the current tree rather than relying on the structure of previous trees, enhancing the model's accuracy and robustness. Additionally, CatBoost employs a gradient-based sorting algorithm that effectively handles missing values, further improving its performance on complex datasets. The objective function in CatBoost is similar to that in XGBoost, with the added flexibility for users to specify whether to perform a second-order Taylor expansion or use the first-order gradient through hyperparameters. This adaptability allows for fine-tuning the model to better capture the underlying patterns in the data.

3. Data collection

In this study, 254 sets of CS data and 210 sets of flexural strength (FS) data for 3DPC were collected in the published

literature (Li 2014, Li 2017, Gu *et al.* 2019, Wang and Gao 2019, Wang 2019a, Wang 2019b, Gu *et al.* 2020, Hou 2020, Cheng 2021, Sun *et al.* 2021, Wu 2021, Yu *et al.* 2021, Zhang *et al.* 2021, Zhu *et al.* 2021, Li and Liao 2022, Sergis *et al.* 2022, Sun *et al.* 2022, Xu 2022, Wang 2022, Wei 2022, Jiang *et al.* 2023, Chen 2023). The two datasets consider 13 input characteristics, including the strength grade and content of ordinary Portland cement and sulphoaluminate cement; the content of fly ash, mineral powder, silica fume, superplasticizer, fiber; water-binder ratio; binder-sand ratio; elastic modulus and length of fiber. The strength of 3DPC is anisotropic due to its layered printing process. There are generally three main orientations to consider, i.e., the orientation perpendicular to the layer, the orientation parallel to the layer, and the direction of the interface between the layers. Vertical strength is usually the lowest, as the bonding between layers is often the weakest link in the structure. Therefore, the CS and FS of 3DPC perpendicular to the direction of the printing layer are selected as the prediction targets. The results of statistical analysis of each variable are shown in Table 1 and Table 2. The histogram of the statistical distribution of the data is shown in Fig. 2.

During data preprocessing, the Min-max normalization technique was introduced to standardize the data. This technique was chosen because it ensures that all features contribute equally to the model and helps in stabilizing the learning process. Each feature was transformed using the following equation

$$X' = \frac{X - X_{\min}}{X_{\max} - X_{\min}} \quad (5)$$

where X' is the normalized data, X is the raw data, and X_{\min} and X_{\max} are the minimum and maximum values of the original data, respectively.

To determine the correlation between the respective variables, the Spearman correlation coefficient was used to measure the degree of correlation between the variables. Fig. 3 illustrates Spearman's correlation matrix. n(W/B) has

Table 3 Results of hyperparameter optimization

Algorithm	Parameters	Range for CS	Optimal CS	Range for FS	Optimal FS
BPANN	hidden layer size	1, 2, 3	2	1, 2, 3	2
	neurons in the hidden layer	[10:1:200]*	(44, 44)	[10 1 200]	(184, 184)
	learning rate	[1e-5:0.0001:0.01]	0.0008	[1e-5 0.0001 0.01]	0.0001
RF	max_depth	[1:1:10]	9	[1:1:10]	9
	min_samples_leaf	0.5, 1, 2, 3	1	0.5, 1, 2, 3	1
	min_samples_split	2, 3, 4, 5	3	2, 3, 4, 5	3
	n_estimators	[10:10:200]	100	[10:10:200]	100
XGBoost	learning rate	0.01, 0.05, 0.1, 0.5	0.1	0.01, 0.05, 0.1, 0.5	0.1
	n_estimators	[10:5:200]	170	[10:5:200]	170
	max_depth	[1:1:10]	4	[1:1:10]	4
CatBoost	max_depth	[1:1:10]	8	[1:1:10]	4
	iterations	[10:10:200]	120	[10:10:200]	100

*In the square brackets, the first number represents the lower bound of the parameter, the last number represents the upper bound of the parameter, and the middle number represents the increment.

Table 4 Performance metrics of each model

Algorithm	Index	CS/Training set	CS/Test set	FS/Training set	FS/Test set
BPANN	MSE (MPa ²)	60.686	131.685	1.883	4.974
	RMSE (MPa)	7.790	11.475	1.372	2.230
	MAE (MPa)	4.602	8.326	0.993	1.422
	R ²	0.939	0.868	0.969	0.902
	EVS	0.939	0.869	0.969	0.903
RF	MSE (MPa ²)	50.095	67.116	2.015	3.565
	RMSE (MPa)	7.078	8.192	1.420	1.888
	MAE (MPa)	4.069	5.788	0.947	1.442
	R ²	0.950	0.927	0.963	0.941
	EVS	0.950	0.932	0.963	0.942
XGBoost	MSE (MPa ²)	47.605	75.957	0.821	3.185
	RMSE (MPa)	6.900	8.715	0.906	1.785
	MAE (MPa)	3.745	5.964	0.549	1.303
	R ²	0.954	0.912	0.983	0.958
	EVS	0.954	0.912	0.983	0.958
CatBoost	MSE (MPa ²)	43.602	61.120	1.256	2.468
	RMSE (MPa)	6.603	7.818	1.121	1.571
	MAE (MPa)	3.108	5.324	0.815	1.123
	R ²	0.958	0.929	0.974	0.967
	EVS	0.958	0.929	0.974	0.967

a strong negative correlation with FS and CS.

4. Modeling

4.1 Performance indicators

In this paper, five model performance evaluation indexes were used, which were mean squared error (MSE), Root Mean Squared Error (RMSE), Mean Absolute Error

(MAE), coefficient of determination (R²) and explained variance score (EVS). MSE serves as a fundamental regression metric, computed as the average of the squared differences between predicted and actual values. RMSE, the square root of MSE, offers straightforward interpretability. MAE computes the average absolute deviation between predicted and actual values, providing a measure of model accuracy. R² assesses the extent to which the model explains the variability in the target variable, with values closer to 1 indicating superior model fit. MAPE functions as

a loss metric, quantifying model evaluation error. EVS gauges how well the model accounts for variance in the target variable, with values nearing 1 indicative of enhanced model performance, offering a comprehensive evaluation of overall model efficacy. The calculation method of each evaluation index is as follows

$$MSE = \frac{1}{n} \sum_{i=1}^n (y_i - \hat{y}_i)^2 \quad (6)$$

$$RMSE = \sqrt{\frac{1}{n} \sum_{i=1}^n (y_i - \hat{y}_i)^2} \quad (7)$$

$$MAE = \frac{1}{n} \sum_{i=1}^n |y_i - \hat{y}_i| \quad (8)$$

$$R^2 = 1 - \frac{\sum_{i=1}^n (y_i - \hat{y}_i)^2}{\sum_{i=1}^n (y_i - \bar{y})^2} \quad (9)$$

$$EVS = 1 - \frac{Var(y_i - \hat{y}_i)}{Var(y_i)} \quad (10)$$

4.2 Modeling process

The dataset is divided into a training set and a test set, with 70% of the data used for model training and parameter tuning, and 30% of the data used to evaluate the performance of the model. Hyperparameters are essential configurations that govern the training process and the architecture of ML models (Bentéjac *et al.* 2021). In contrast to model parameters, which are derived from the data during training, hyperparameters must be predetermined before the commencement of training. In this study, the grid search method combined with a five-fold cross-validation was used to determine the optimal combination of hyperparameters on the training set. All ML models were implemented and executed using Python. Table 3 shows the results of hyperparameter optimization. Upon training the model, predictions are generated for the test set, and the performance of each model is comprehensively evaluated using metrics such as R^2 , MSE, RMSE, MAE, and EVS.

4.3 Model performance evaluation

4.3.1 CS prediction

The performance indicators for four ML models to predict the 28-day CS of 3DPC are shown in Table 4. CatBoost model achieves an R^2 value of 0.958 and an RMSE of 6.603 MPa for the training set, and an R^2 of 0.929 with an RMSE of 7.818 MPa for the test set. These metrics indicate that CatBoost outperforms the other three models, showcasing its superior ability to generalize from the training data to the test data. The lower RMSE values reflect its higher accuracy in predicting CS, thereby validating its robustness and effectiveness as a predictive model. This can be attributed to CatBoost's randomized gradient boosts and symmetric trees enhancing stability and accuracy, fewer hyperparameter adjustments simplifying tuning and improving performance with large datasets, and the Ordered Boosting technique increasing model flexibility

and adaptability. The prediction performance of XGBoost and RF models was satisfactory, demonstrated by an R^2 of 0.954, RMSE of 6.900 MPa for the XGBoost training set and an R^2 of 0.912, RMSE of 8.715 MPa for the test set. Similarly, the RF model yielded an R^2 of 0.950, RMSE of 7.078 MPa for the training set, and an R^2 of 0.927, RMSE of 8.192 MPa for the test set. The efficacy of XGBoost and RF, both of which are ensemble learning algorithms, is attributed to their ability to exploit the relationships between data features and multiple weak learners, as well as their flexibility in parameter tuning, which collectively enhance the predictive performance of the models. Compared with the first three tree-based ensemble models, the prediction performance of the BPANN is relatively poor, exhibiting an R^2 value of 0.939 in the training set and 0.868 in the test set, which indicates a lower generalization performance. This suggests that BPANN is less effective in capturing the underlying patterns in the data and may overfit the training data, resulting in diminished predictive accuracy on unseen data. BPANN algorithms typically require a large amount of training data to learn model parameters efficiently, especially when dealing with high-dimensional sparse data (Bishop 2006, Hinton *et al.* 2012, Rumelhart *et al.* 1986). However, for the tree model, the splitting process of the tree only needs to consider the value of a single feature and does not need to consider the combination of all features at the same time. This feature makes the tree model more efficient when dealing with high-dimensional sparse data (Breiman 2001). Chen *et al.* (2016) argued that column sampling is one of the effective methods to deal with sparsity and zero-value problems. This approach builds each tree by randomly selecting a subset of features (columns), which reduces the risk of overfitting and enhances the generalization ability of the model.

Fig. 4 illustrates the fitting results of the predicted values from the four ML models compared to the experimental values for both the training set and the test set. The distribution of data points for the CatBoost, XGBoost, and RF models is quite similar. Moreover, the data points for these three models are more closely clustered around the $y=x$ line, indicating a better fit, compared to the BPANN model, whose data points show greater dispersion from the $y=x$ line. For the RF, XGBoost, and CatBoost models, over 80% of the points fall within the regions bounded by the two reference lines ($\pm 15\%$), whereas only 74.4% of the points do so for the BPANN model. This further emphasizes the superior predictive accuracy and generalization capabilities of the tree-based ensemble models over the BPANN model.

To comprehensively evaluate the performance of ML models across different strength ranges, a detailed analysis was conducted to identify the strengths and weaknesses of each model in different application scenarios, providing valuable insights for model improvement and optimization (Ali *et al.* 2023, Ibrahim *et al.* 2023). Table 5 presents the performance of different models across three CS ranges. In the low-intensity range (10–80 MPa), the BPANN model demonstrates poor performance with an R^2 of 0.552, while the RF model performs better but still shows limited predictive ability. XGBoost and CatBoost models exhibit

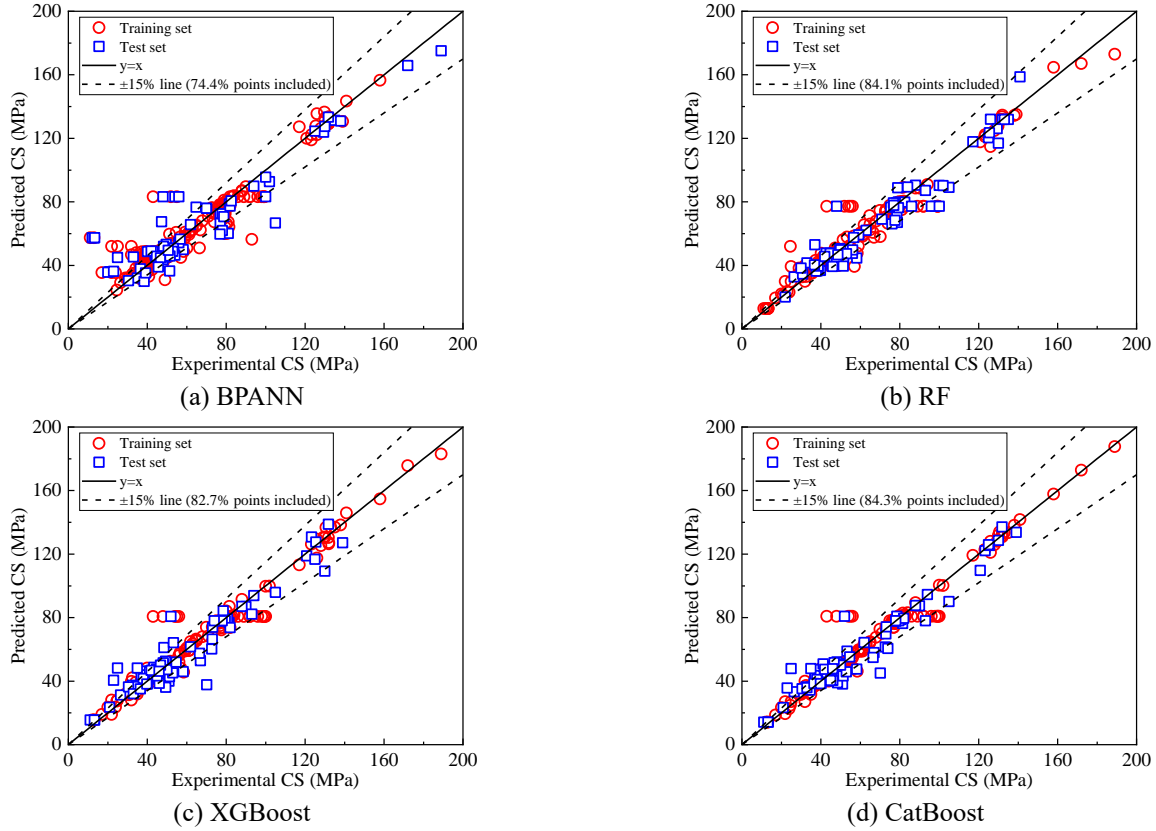


Fig. 4 Performance of ML models to predict the CS

Table 5 Performance comparison of ML models in different CS ranges

Algorithm	Range (MPa)	Number	MSE (MPa ²)	RMSE (MPa)	MAE (MPa)	R ²	EVS	Remarks
BPANN	10-80	194	133.842	11.577	7.158	0.552	0.554	Poor
	80-130	47	109.018	10.448	8.397	0.663	0.735	Poor
	130-190	15	50.303	7.095	5.791	0.834	0.837	Good
RF	10-80	194	70.254	8.384	5.192	0.767	0.778	Good
	80-130	47	68.536	8.286	6.344	0.799	0.879	Good
	130-190	15	87.377	9.355	5.535	0.708	0.798	Poor
XGBoost	10-80	194	52.538	7.258	3.703	0.825	0.832	Good
	80-130	47	46.417	6.812	4.828	0.862	0.893	Good
	130-190	15	57.035	7.551	4.793	0.803	0.834	Good
Catboost	10-80	194	49.481	7.035	3.852	0.832	0.848	Good
	80-130	47	66.490	8.156	5.431	0.796	0.879	Good
	130-190	15	5.754	2.408	1.919	0.984	0.986	Very Good

strong performance, with CatBoost achieving an R^2 of 0.832 and an EVS of 0.848. In the medium-intensity range (80-130 MPa), the BPANN model shows some improvement but remains suboptimal with an R^2 of 0.663. The RF model performs reasonably well, achieving an R^2 of 0.799, while XGBoost shows further improvement with an R^2 of 0.862. CatBoost maintains strong predictive power with an EVS of 0.879. In the high-intensity range (130-190 MPa), the BPANN model achieves good but not ideal performance with an R^2 of 0.834. The RF model's performance decreases in this range with an R^2 of 0.708,

whereas XGBoost maintains strong performance with an R^2 of 0.803. The CatBoost model excels, providing highly accurate predictions with an R^2 of 0.984 and an EVS of 0.986.

4.3.2 FS prediction

The results of the FS prediction model are presented in Table 4. XGBoost model demonstrated the highest performance in the training set, achieving an R^2 of 0.983 and an RMSE of 0.906 MPa. CatBoost model exhibited the best performance in the test set, with an R^2 of 0.967 and an

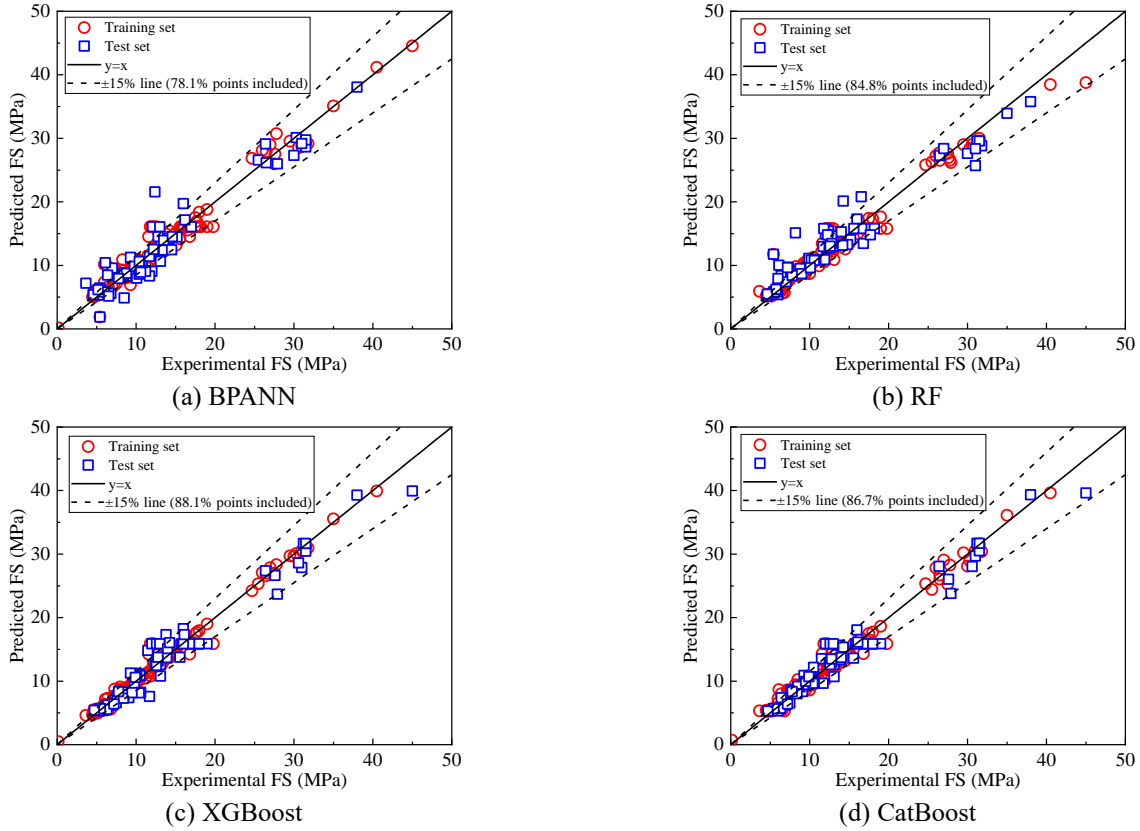


Fig. 5 Performance of ML models to predict the FS

Table 6 Performance comparison of ML models in different FS ranges

Algorithm	Range (MPa)	number	MSE (MPa ²)	RMSE (MPa)	MAE (MPa)	R ²	EVS	Remarks
BPANN	0.14-15	160	3.11	1.76	1.14	0.68	0.68	Poor
	15-30	39	2.46	1.57	1.24	0.90	0.92	Very Good
	30-50	14	3.02	1.74	1.45	0.84	0.93	Good
RF	0.14-15	194	1.92	1.39	0.96	0.80	0.82	Good
	15-30	47	4.70	2.17	1.54	0.82	0.86	Good
	30-50	15	3.53	1.88	1.54	0.82	0.83	Good
XGBoost	0.14-15	194	52.53	7.25	3.70	0.82	0.83	Good
	15-30	47	1.25	1.12	0.69	0.87	0.87	Good
	30-50	15	3.16	1.78	1.09	0.88	0.89	Good
CatBoost	0.14-15	194	1.02	1.01	0.64	0.89	0.90	Good
	15-30	47	2.60	1.61	1.06	0.90	0.92	Very Good
	30-50	15	3.28	1.81	1.14	0.83	0.87	Good

RMSE of 1.571 MPa. These results highlight the exceptional capability of XGBoost to fit the training data with minimal error, while CatBoost excels in generalizing to the test data, maintaining a strong predictive performance with lower error margins compared to the other models. Despite a slight overfitting issue observed in the BPANN model, the R^2 values for both the training and test sets exceeded 0.9, indicating reasonable predictive capability. Similarly, the RF model achieved R^2 values of 0.930 for the training set and 0.941 for the test set, both surpassing the 0.9 threshold. Fig. 5 displays the fitting results of the

predicted values from the four bending models against the experimental values for both the training and test sets. The data points for the CatBoost, XGBoost, RF, and BPANN models are densely clustered around the $y=x$ line. In the case of the RF, XGBoost, and CatBoost models, more than 80% of the data points are located within the $\pm 15\%$ boundary defined by the reference lines, whereas the BPANN model has 78.1% of its data points within this range.

Table 6 details the model performance across different FS ranges. CatBoost excels across all ranges, with

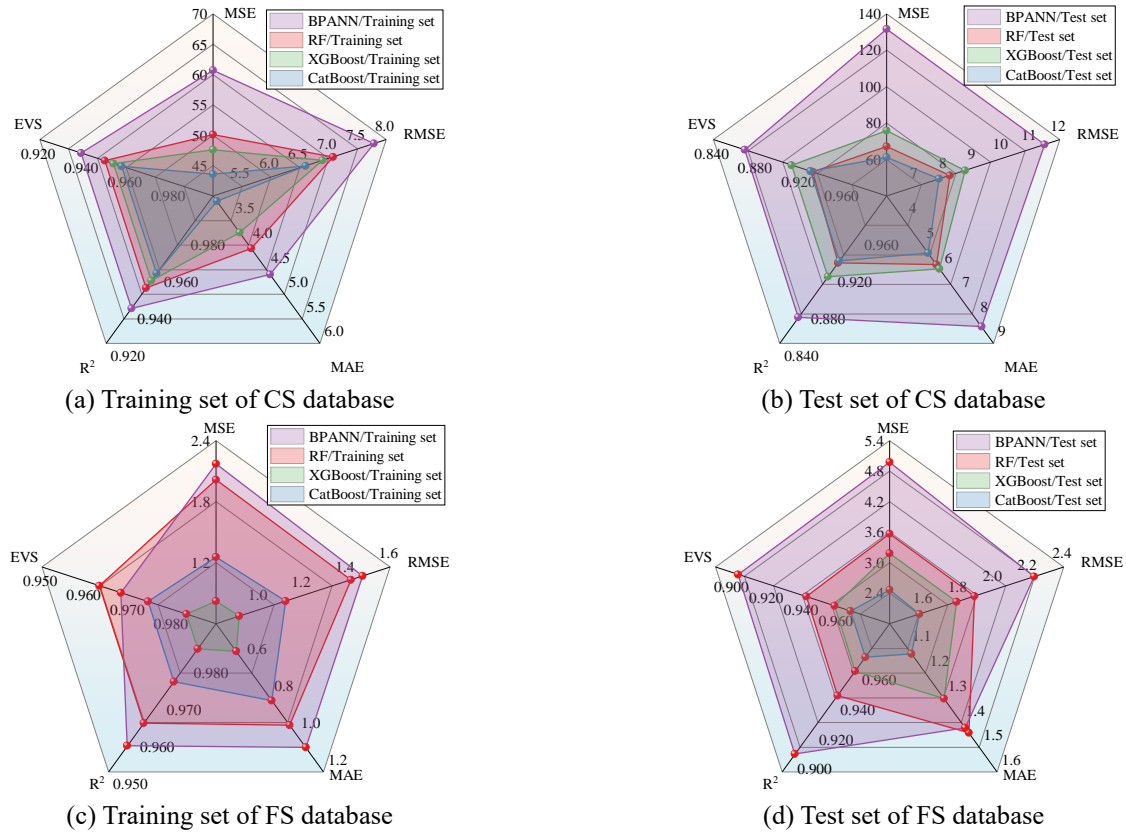


Fig. 6 Radar charts for all datasets

particularly strong performance in the medium strength range (15-30 MPa), indicating excellent predictive ability. In the low strength range (0.14-15 MPa), CatBoost also performs well. Although its performance shows a slight decrease in the high strength range (30-50 MPa), it remains robust. The BP model shows varied performance: poor in the low strength range, but very good in the medium range. Its performance slightly drops in the high range. The RF model performs well in the low strength range and maintains high performance in the medium and high strength ranges. XGBoost has average performance in the low strength range but shows improved predictive ability in the medium and high strength ranges.

Fig. 6 presents the radar charts for all datasets, which provide a comprehensive evaluation of the ML models' performance differences based on the area enclosed by the results of indicators. A smaller area indicates better performance, while a larger area suggests poorer performance. For the CS series model, CatBoost has the smallest area in both the training set and the test set graphs, signifying the best overall performance. Conversely, the BPANN exhibits the largest area in both plots, indicating the worst performance. The areas for the XGBoost and RF models lie between those of CatBoost and BPANN, but they are closer to CatBoost, reflecting their relatively strong performance. For the FS series model, CatBoost again shows the smallest area in the training set, followed by XGBoost. However, in the test set, XGBoost has the smallest area, with CatBoost closely following. Both models demonstrate their strengths in the training and test

sets, underscoring their reliable predictive capabilities. Overall, based on the results of the compressive and FS prediction performance, CatBoost demonstrates high-precision prediction performance and robust generalization ability.

4.4 Model interpretability

Interpretability analysis focuses on understanding the underlying mechanisms and decision-making processes of the model. The CatBoost model has exhibited superior performance compared to the other models in predicting the mechanical performance of 3DPC. Then, this section undertakes an in-depth analysis of the interpretability of the CatBoost model to further substantiate its applicability. The interpretability analysis in this study involves a comprehensive examination of SHAP and PDPs.

4.5 SHAP analysis

4.5.1 Global analysis

Feature importance analysis identifies the most significant variables influencing the model's predictions, providing insights into the critical factors affecting compressive and FS in 3DPC. Fig. 7 and Fig. 8 display the feature importance of the input variables for CS and FS, respectively. The color of the dots ranging from blue to red, indicates eigenvalues from low to high. The X-axis represents the SHAP value, with higher values signifying a greater influence of the feature on the prediction. The SHAP

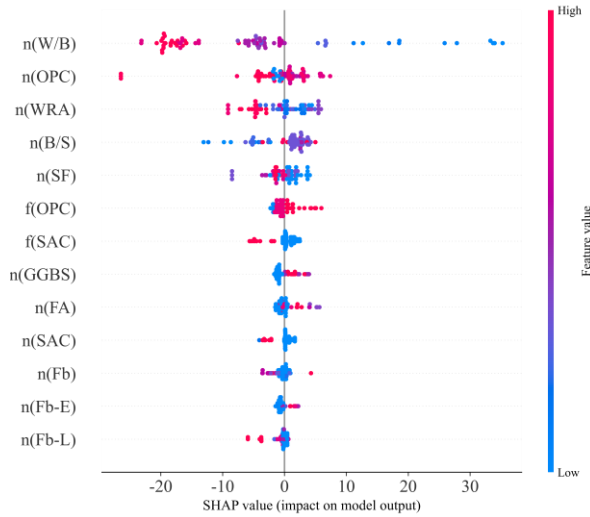


Fig. 7 CatBoost for CS

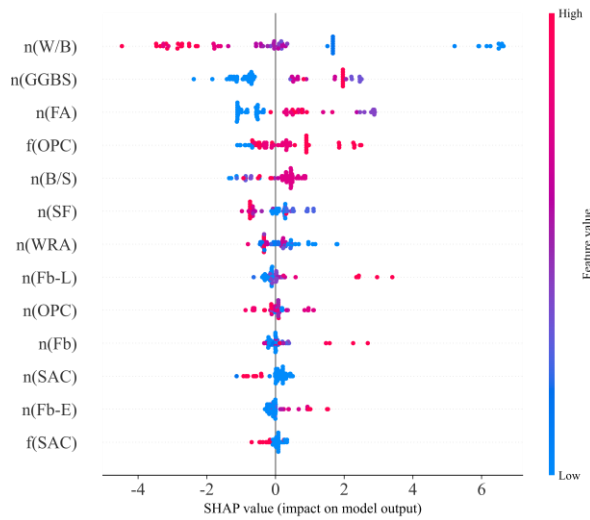


Fig. 8 CatBoost for FS

values of the features are primarily distributed on the right side of the mean value, indicating that the SHAP values are close to positive, thereby having a positive impact on the results. Conversely, SHAP values on the left side indicate negative influences.

As shown in Fig. 7, the $n(W/B)$ exhibits the highest feature importance in predicting the CS of 3DPC. The features $n(OPC)$, $n(B/S)$, $n(WRA)$, $n(SF)$, and $f(OPC)$ also significantly influence CS predictions. Specifically, the SHAP values for $n(OPC)$, $n(B/S)$, and $f(OPC)$ are predominantly distributed on the right side of the mean value, indicating a positive correlation with CS. Conversely, the SHAP values for $n(W/B)$, $n(WRA)$, and $n(SF)$ are primarily close to negative, suggesting that higher values of these features correlate with lower CS. Excessive $n(W/B)$ increases porosity, leading to less dense concrete and reduced strength (J 2021). Additionally, the SHAP values for $n(Fb)$, $n(Fb-E)$, and $n(Fb-L)$ are nearly zero, indicating minimal impact on the model's output. It should be noted that an increase in $n(SF)$ results in a decrease in CS, contrary to observations in conventional concrete. This

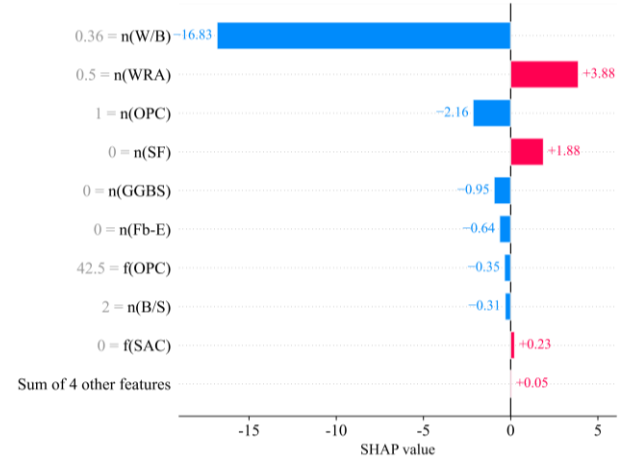


Fig. 9 Waterfall of the sample 11 (Li 2014)

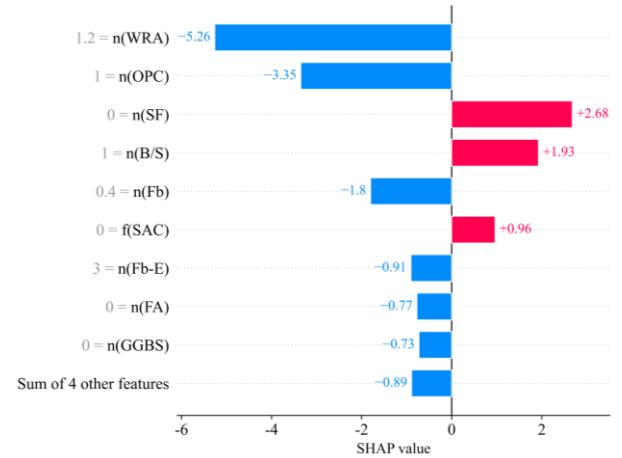


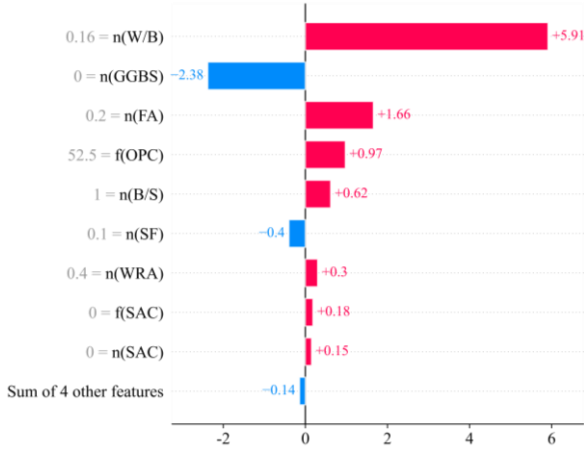
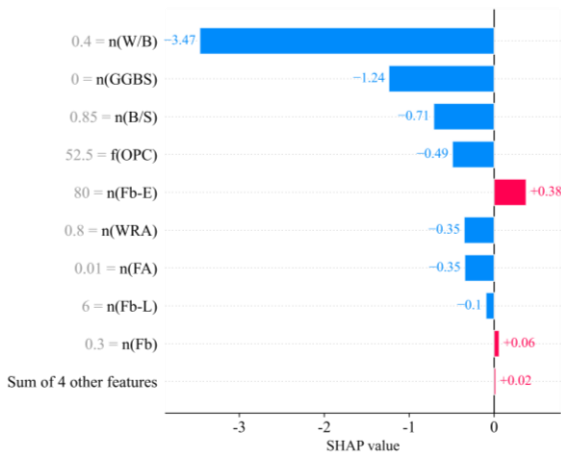
Fig. 10 Waterfall of the sample P8L12 (Cheng 2021)

discrepancy may be due to the typically lower W/B ratio used in 3DPC, where higher $n(SF)$ reduces fluidity. The large specific surface area of silica fume significantly adsorbs water, reducing the availability of free water and consequently decreasing CS (Sun *et al.* 2021).

Fig. 8 illustrates that $n(W/B)$ is the most important feature in predicting FS of 3DPC. Other features such as $n(GGBS)$, $n(FA)$, $f(OPC)$, $n(B/S)$, and $n(SF)$ significantly impact the FS prediction results. Among these, the SHAP values for $n(GGBS)$, $n(FA)$, $f(OPC)$, and $n(B/S)$ are predominantly positive, indicating a positive effect on FS. In contrast, the SHAP values for $n(W/B)$ and $n(SF)$ are primarily negative, suggesting that higher values of these features correlate with lower FS.

4.5.2 Local analysis

Fig. 9 and Fig. 10 present the waterfall plots for two samples within the CS database. Each waterfall plot begins with the expected value of the model output, and subsequent rows illustrate the positive (red) or negative (blue) contributions of each feature. Sample 11 exhibits $n(W/B)$ as the predominant factor influencing CS, while sample P8L12 demonstrates that $n(WRA)$ plays a pivotal role in determining CS. It is observed that the feature importance of most variables aligns with the global feature

Fig. 11 Waterfall of the sample 6 (Sun *et al.* 2021)Fig. 12 Waterfall of the sample 3 (Yu *et al.* 2021)

importance. However, certain individual variables exhibit an opposite trend compared to the global change pattern. For example, the value of $n(WRA)$ in Fig. 9 is 0.5, which is below the average. Conversely, in Fig. 10, $n(WRA)$ has a value of 1.2, which is above the average, indicating a strong negative impact consistent with the global characteristic trend. Then, the $n(WRA)$ must be maintained within an optimal range, as an excessive dosage may lead to a reduction in strength. This also emphasizes the need for tailored adjustments based on specific sample values rather than relying solely on global feature importance.

Moreover, in Fig. 9 and Fig. 10, certain data points manifest eigenvalues of 0, yet their SHAP values are computationally viable. This outcome arises from SHAP value computations, which encompass not only the discrete feature value but also its marginal impact on the model's prediction. Thus, even in instances where particular feature values are nullified, the SHAP methodology remains proficient in offering substantive insights into the potential influence of these features on the output. This highlights the robustness of SHAP analysis in facilitating a comprehensive comprehension of feature contributions, irrespective of their precise manifestations within the dataset.

Fig. 11 and Fig. 12 present the waterfall plots for two additional samples within the FS database. In Fig. 11, the

$n(W/B)$ result indicates a positive effect, which contrasts with the global analysis. Specifically, while the average size of $n(W/B)$ in the FS database is 0.29, the corresponding case in Fig. 11 has a size of 0.16, which is below the average. In contrast, the $n(W/B)$ size in Fig. 12 is 0.4, exceeding the average, thus demonstrating a strong negative effect consistent with the global characteristic trend. Likewise, the average $n(FA)$ in the FS database stands at 0.07, while it is 0.01 in the case depicted in Fig. 12, falling below the average. Conversely, in Fig. 11, the $n(FA)$ reaches 0.2, surpassing the average and indicating a pronounced positive effect that aligns with the overall characteristic trend. In Fig. 12, the contribution of $n(GGBS)$ is negative, despite the overall effect being positive. This discrepancy arises because the $n(GGBS)$ of 0 in the specific case is lower than the dataset average of 0.08.

4.5.3 PDPs analysis

PDPs illustrate the marginal effect of each feature on the outcome, providing valuable insights into the relationships between features and predictions. Fig. 13 displays the results of the main variables affecting CS in one-way PDPs. Both $n(W/B)$ and $n(WRA)$ negatively impact CS, as their increasing values correspond to decreasing dependence on CS. Conversely, $f(OPC)$ and $n(B/S)$ positively influence the outcome, with higher values leading to an overall increase in the dependence. This finding aligns with the results derived from the SHAP global analysis. The $n(W/B)$ maintains a high dependence of approximately 90 within the range of 0 to 0.16; however, beyond 0.16, its dependence drops sharply. Once $n(W/B)$ exceeds 0.35, the dependence stabilizes around 50. The $n(B/S)$ sees its dependence rise rapidly from 54.5 to 64.5 within the range of 0 to 0.9, with only a slight subsequent decline, eventually stabilizing overall. For $n(WRA)$, the dependence decreases as the superplasticizer content increases from 0 to 1.23, but stabilizes once the content exceeds 1.23.

Fig. 14 illustrates the results of the main variables affecting FS using one-way PDPs. The variable $n(W/B)$ negatively impacts FS, as higher values correspond to reduced dependence. Conversely, $f(OPC)$ and $n(GGBS)$ exhibit a positive effect on FS, with increasing values leading to higher dependence, consistent with the SHAP analysis results. The trend for $f(OPC)$ mirrors that observed for CS. The dependence on $n(W/B)$ remains high up to a value of 0.16, beyond which it decreases sharply; however, when $n(W/B)$ exceeds 0.35, the dependence levels off. For $n(FA)$, within the range of 0 to 0.1, the dependence increases rapidly from 12.5 to 14.0, then gradually decreases, stabilizing once $n(FA)$ exceeds 0.3. The dependence on $n(GGBS)$ rises swiftly to 13.5 when $n(GGBS)$ is between 0 and 0.08 and then stabilizes at around 13.5.

To further examine the influence of multivariate interactions on the outputs, several variables with high feature importance were selected for two-way PDPs. Two-way PDPs provide valuable insights by visualizing and analyzing the model's behavior through multidimensional feature combinations. The results of the two-way PDPs for CS are presented in Fig. 15. When $n(W/B)$ exceeds 0.3,

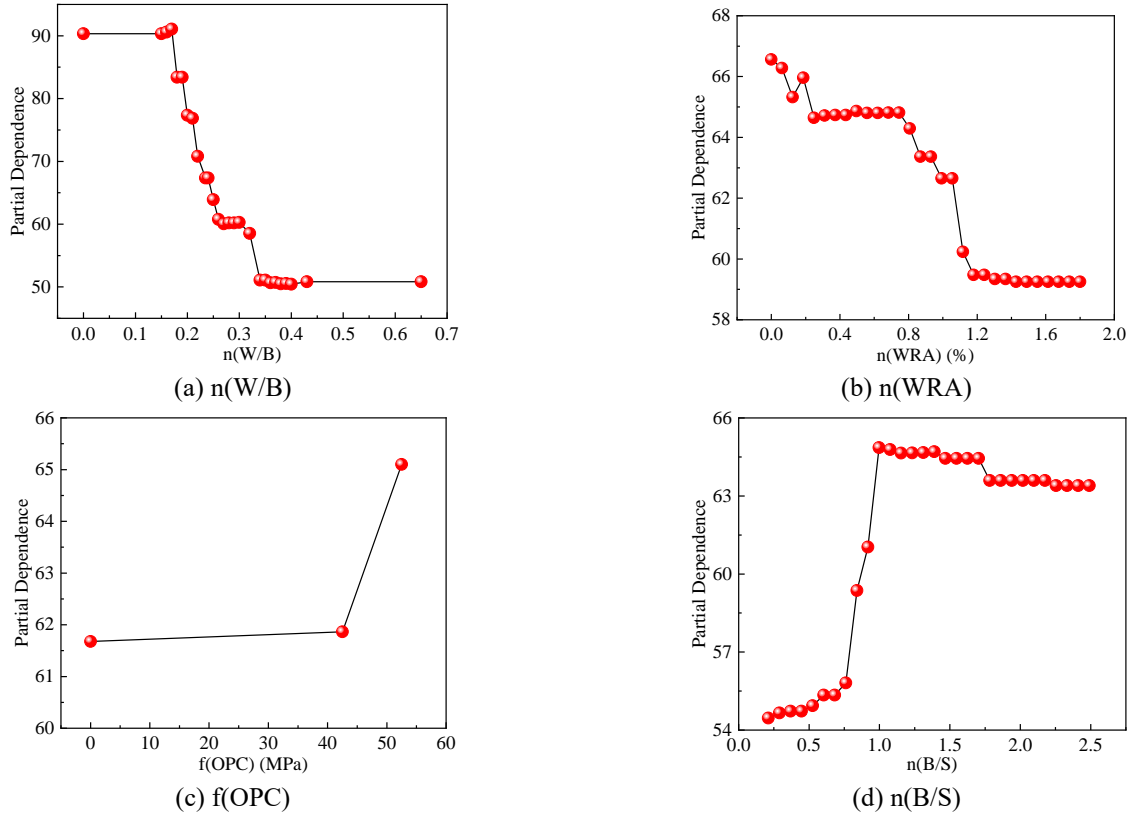


Fig. 13 One-way PDPs for the CS database

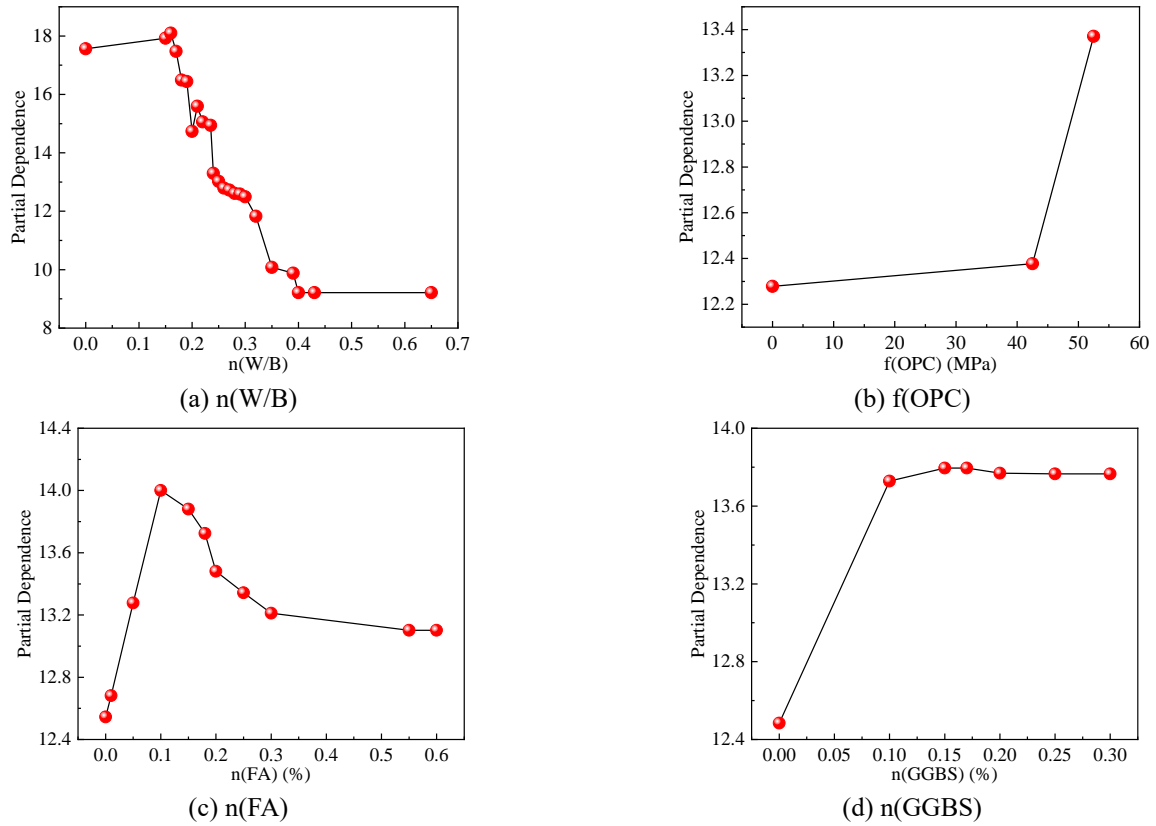


Fig. 14 One-way PDPs for the FS database

neither $n(W/B)$ nor $n(WRA)$ significantly affect CS. Conversely, when $n(W/B)$ is below 0.3, both $n(W/B)$ and

$n(WRA)$ exert significant effects on CS. When $n(W/B)$ is less than 0.1, the dependence surface slope is highly

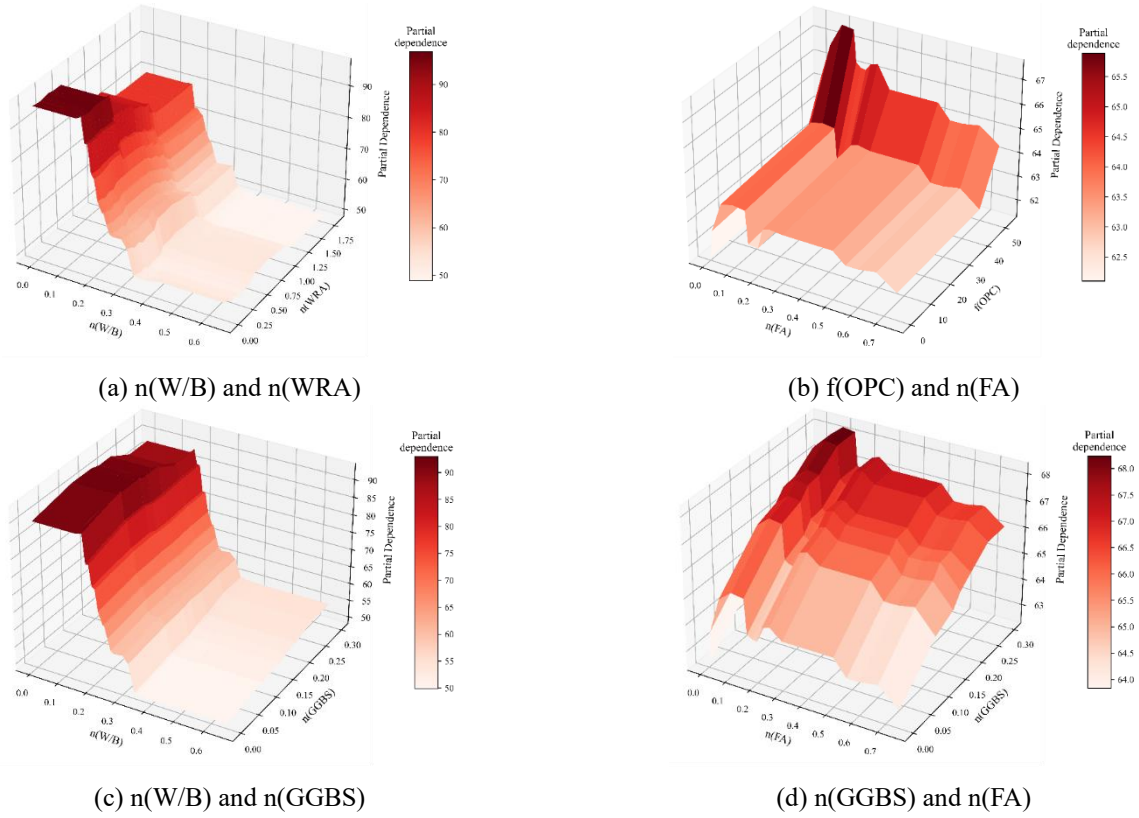


Fig. 15 Two-way PDPs for the CS database

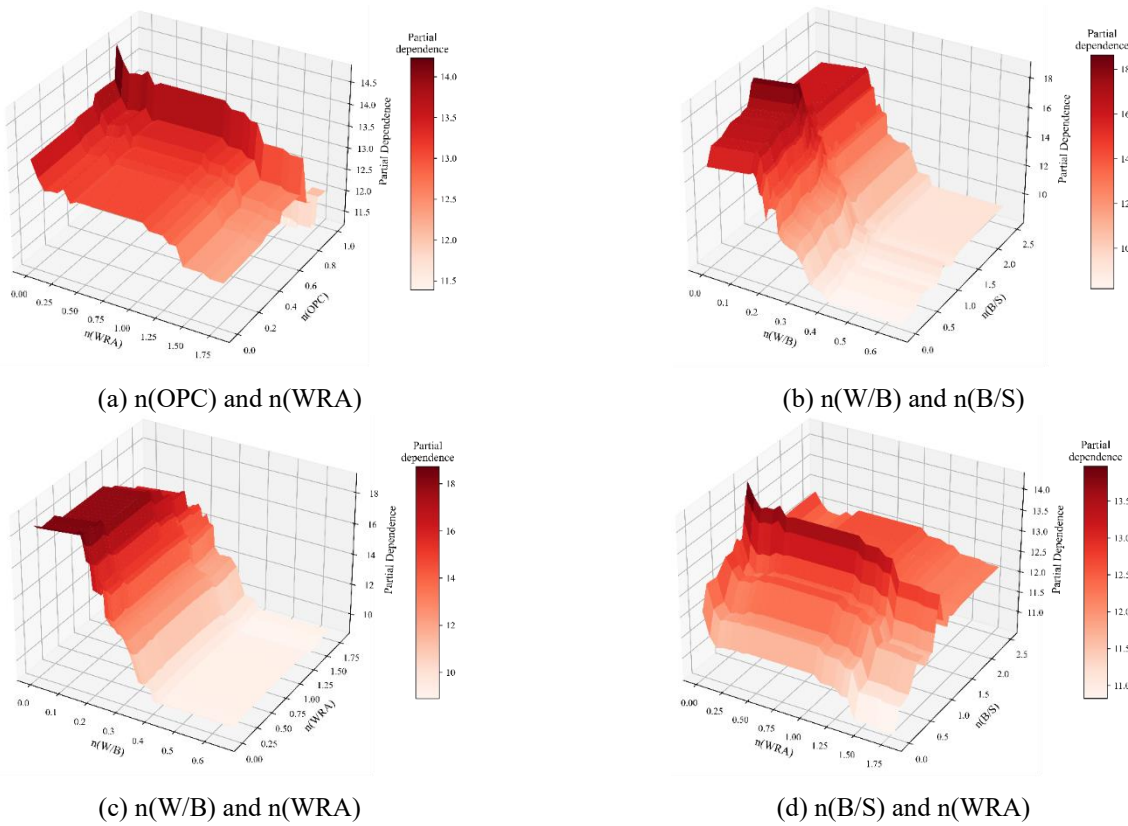


Fig. 16 Two-way PDPs for the FS database

dependent on $n(WRA)$. At the $f(OPC)$ value of 42.5 MPa, the dependence surface is smooth when $n(FA)$ is between

0.2 and 0.4, but steeper elsewhere. For $n(W/B)$ values above 0.35, neither $n(W/B)$ nor $n(GGBS)$ significantly

affect CS. However, when $n(W/B)$ is below 0.3, both variables strongly influence CS. Regarding the interaction between $n(GGBS)$ and $n(FA)$, increasing their values consistently has a strong positive impact on CS across all intervals. However, when $n(FA)$ is around 0.3, there is a sharp decrease in CS.

The findings from the analysis of two-way PDPs for FS are illustrated in Fig. 16. When the $n(OPC)$ was below 0.7, it did not exhibit a notable impact on the FS, whereas $n(WRA)$ demonstrated a substantial effect. As $n(OPC)$ approaches 0.7, there is a significant increase in dependence. However, when $n(OPC)$ exceeds 0.8, there is a sharp decline in dependence. When $n(W/B)$ exceeded 0.4, neither $n(W/B)$ nor $n(B/S)$ significantly affected FS. Conversely, when $n(W/B)$ was below 0.4, both $n(W/B)$ and $n(B/S)$ exhibited certain effects on FS. With $n(W/B)$ exceeding 0.3, neither $n(W/B)$ nor $n(WRA)$ significantly affected FS. In contrast, when $n(W/B)$ fell below 0.3, both $n(W/B)$ and $n(WRA)$ displayed significant effects on FS, particularly $n(W/B)$, which exhibited a substantial impact. The slope of dependence with a threshold of $n(W/B)$ at 0.15 is highly dependent on $n(WRA)$. When $n(B/S)$ exceeded 1.25, $n(WRA)$ still had some impact on the FS, whereas $n(B/S)$ did not exert a significant influence. On the other hand, when $n(B/S)$ was less than 1.25, $n(B/S)$ strongly influenced FS, with $n(WRA)$ only exerting a certain influence in specific intervals. At approximately $n(B/S)$ of 1.0, the dependence increases and reaches a peak, with the slope experiencing a sharp increase followed by a decrease.

5. Conclusions

This study investigates predicting the mechanical properties of 3DPC utilizing well-trained ML models. A comprehensive database was created by aggregating experimental data from studies reported in the literature, encompassing results from 254 sets of CS data and 210 sets of FS data. The performance of four ML models was compared to optimize the predictive model. Consequently, model interpretability was examined using SHAP and PDPs. Based on the results and analysis, the following conclusions are drawn:

- Ensemble algorithms based on tree models, such as RF, XGBoost, and CatBoost, may offer significant advantages over BPANN in predicting the mechanical performance of 3DPC. This is attributed to the inherent capability of tree-based ensemble methods to handle complex interactions and non-linear relationships within the data more effectively, particularly with high-dimensional data.
- Among the models for predicting CS, CatBoost achieved an R^2 of 0.958 and an RMSE of 6.603 MPa for the training set, and an R^2 of 0.929 with an RMSE of 7.818 MPa for the test set, outperforming the other models. For the models predicting FS, the XGBoost model demonstrates the highest performance on the training set, achieving an R^2 of 0.983 and an RMSE of 0.906 MPa. On the test set, the CatBoost model exhibited the best performance, with an R^2 of 0.967 and an RMSE of 1.571 MPa.

- SHAP analysis identified the $n(W/B)$ as a critical factor influencing the mechanical properties of 3DPC. Excessive superplasticizers can degrade the mechanical properties of 3DPC. PDPs analysis reveals that the impact of the $n(WRA)$ on CS exhibits a negative influence initially, which gradually diminishes in significance as it increases. When $n(W/B)$ exceeded 0.4, neither $n(W/B)$ nor $n(B/S)$ demonstrated significant effects on FS.

While models with good predictive performance for the mechanical properties of 3DPC were successfully developed in this study, several limitations were identified. For instance, the dataset used potentially constrains the generalizability of the models, particularly with the incorporation of novel materials such as lime powder. Efforts are underway to collect an expanded dataset that includes new materials for future training endeavors. Additionally, it is recognized that the quality of 3DPC extends beyond its mechanical attributes to include crucial rheological properties. With the completion of mechanical properties modeling, forthcoming research should shift focus toward predicting the flow characteristics of 3DPC.

Acknowledgments

The research described in this paper was financially supported by the National Natural Science Foundation of China (No. 52108123).

Data availability

All data are available at <https://github.com/Marvin-LiJunZan/Machine-learning-driven-prediction-of-mechanical-properties-for-3D-printed-concrete.git>.

References

- Ahmed, H.U., Abdalla, A.A., Mohammed, A.S. and Mohammed, A.A. (2022), "Mathematical modeling techniques to predict the compressive strength of high-strength concrete incorporated metakaolin with multiple mix proportions", *Clean. Mater.*, **5**, 100132. <https://doi.org/10.1016/j.clema.2022.100132>.
- Ahmed, H.U., Mohammed, A.S., Mohammed, A.A. and Faraj, R.H. (2021), "Systematic multiscale models to predict the compressive strength of fly ash-based geopolymer concrete at various mixture proportions and curing regimes", *Plos One*, **16**, e0253006. <https://doi.org/10.1371/journal.pone.0253006>.
- Ali, A., Riaz, R.D., Malik, U.J., Abbas, S.B., Usman, M., Shah, M.U., Kim, I.H., Hanif, A. and Faizan, M. (2023), "ML-based predictive model for tensile and flexural strength of 3D printed concrete", *Mater.*, **16**, 4149. <https://doi.org/10.3390/ma16114149>.
- Ali, R., Muayad, M., Mohammed, A.S. and Asteris, P.G. (2023), "Analysis and prediction of the effect of Nanosilica on the compressive strength of concrete with different mix proportions and specimen sizes using various numerical approaches", *Struct. Concrete*, **24**(3), 4161-4184. <https://doi.org/10.1002/suco.202200718>.
- Anitescu, C., Atroshchenko, E., Alajlan, N. and Rabczuk, T. (2019), "Artificial neural network methods for the solution of

- second order boundary value problems”, *Comput. Mater. Contin.*, **59**(1), 345-359. <https://doi.org/10.32604/cmc.2019.06641>.
- Bentéjac, C., Csörgő, A. and Martínez-Muñoz, G. (2021), “A comparative analysis of gradient boosting algorithms”, *Artif. Intell. Rev.*, **54**, 1937-1967. <https://doi.org/10.1007/s10462-020-09896-5>.
- Bishop, C.M. (2006), *Neural Networks in Pattern Recognition and ML*, Springer, New York, NY, USA.
- Breiman, L. (2001), “Random forests”, *Mach. Learn.*, **45**, 5-32. <https://doi.org/10.1023/A:1010933404324>.
- Chen, C. (2023), “Research on the effect of ceramic sand on the printability and mechanical behavior of 3D printing mortar”, Master’s Degree Thesis, Shandong Agricultural University, Shandong, China. <https://doi.org/10.27277/d.cnki.gsdnu.2022.000376>.
- Chen, T. and Guestrin, C. (2016), “XGBoost: A scalable tree boosting system”, *Proceedings of the 22nd ACM SIGKDD International Conference on Knowledge Discovery and Data Mining*, San Francisco, CA, USA.
- Cheng, X. (2021), “Research on the preparation and crack resistance of 3D printed fiber reinforced concrete”, Master’s Degree Thesis, Hebei University of Technology, Tianjin, China.
- Choudhary, L., Sahu, V., Dongre, A. and Garg, A. (2024), “Prediction of compressive strength of sustainable concrete using machine learning tools”, *Comput. Concrete*, **33**(2), 137-145. <https://doi.org/10.12989/CAC.2024.33.2.137>.
- Dilawar Riaz, R., Usman, M., Ali, A., Majid, U., Faizan, M. and Jalil Malik, U. (2023), “Inclusive characterization of 3D printed concrete (3DPC) in additive manufacturing: A detailed review”, *Constr. Build. Mater.*, **394**, 132229. <https://doi.org/10.1016/j.conbuildmat.2023.132229>.
- Garg, A., Aggarwal, P., Aggarwal, Y., Belarbi, M.O., Chalak, H.D., Tounsi, A. and Gulia, R. (2022), “Machine learning models for predicting the compressive strength of concrete containing nano silica”, *Comput. Concrete*, **30**(1), 33-42. <https://doi.org/10.12989/cac.2022.30.1.033>.
- Gomaa, E., Han, T., ElGawady, M., Huang, J. and Kumar, A. (2021), “ML to predict properties of fresh and hardened alkali-activated concrete”, *Cement Concrete Compos.*, **115**, 103863. <https://doi.org/10.1016/j.cemconcomp.2020.103863>.
- Goswami, S., Anitescu, C., Chakraborty, S. and Rabczuk, T. (2020), “Transfer learning enhanced physics informed neural network for phase-field modeling of fracture”, *Theoret. Appl. Fract. Mech.*, **106**, 102447. <https://doi.org/10.1016/j.tafmec.2019.102447>.
- Gu, H., Jia, T., Song, H., Gu, F., Yang, H., Che, Y. and Yan, S. (2019), “Experimental study on 3D printing of phosphate slag powder concrete”, *J. Guizhou Normal Univ. (Nat. Sci. Ed.)*, **37**, 77-84. <https://doi.org/10.16614/j.gznj.zrb.2019.05.013>.
- Gu, H., Sun, J., Zhang, J., Xu, Y., Li, B. and Wu, W. (2020), “Effect of material ratio on the performances in 3D cement printing and its optimization”, *AIP Adv.*, **10**, 125012. <https://doi.org/10.1063/5.0030186>.
- Hinton, G., Li, D., Yu, D., Dahl, G., Mohamed, A., Jaitly, N., Senior, A., Vanhoucke, V., Nguyen, P., Sainath, T. and Kingsbury, B. (2012), “Deep neural networks for acoustic modeling in speech recognition”, *IEEE Signal Pr. Mag.*, **29**(6), 82-97. <https://doi.org/10.1109/MSP.2012.2205597>.
- Hou, Z. (2020), “Research on the preparation and properties of 3D printed fiber reinforced concrete”, Master’s Degree Thesis, Southeast University, Jiangsu, China.
- Ibrahim, A.K., Dhahir, H.Y., Mohammed, A.S., Omar, H.A. and Sedo, A.H. (2023), “The effectiveness of surrogate models in predicting the long-term behavior of varying compressive strength ranges of recycled concrete aggregate for a variety of shapes and sizes of specimens”, *Arch. Civil Mech. Eng.*, **23**(1), 61. <https://doi.org/10.1007/s43452-022-00595-2>.
- Jiang, Q., Wu S, Liu, Q., Xin, J. and Zheng, H. (2023), “Cement-based 3D printing material foundation mix ratio test and quality evaluation”, *Rock Soil Mech.*, **44**, 1245-1259. <https://doi.org/10.16285/j.rsm.2022.0824>.
- Li, B. and Liao, B. (2022), “Study on 3D printing mechanical properties of PVA fiber reinforced iron tailings concrete”, *Metal Min.*, **2022**, 59-64. <https://doi.org/10.19614/j.cnki.jsks.202212009>.
- Li, J. (2021), “Numerical study on the effect of chloride salt erosion on the mechanical properties of concrete components”, Master’s Degree Thesis, Xi’an University of Architecture and Technology, Xi’an, China.
- Li, T. (2017), “Application of recycled fine aggregate concrete in 3D printing construction”, Master’s Degree Thesis, Hanoi University of Science and Technology, Hà Nội, Vietnam.
- Li, X. (2014), “Research on the design of 3D printed concrete mix ratio and its basic properties”, Master’s Degree Thesis, Hanoi University of Science and Technology, Hà Nội, Vietnam.
- Liu, K., Takasu, K., Jiang, J., Zu, K. and Gao, W. (2023), “Mechanical properties of 3D printed concrete components: A review”, *Dev. Built Environ.*, **16**, 100292. <https://doi.org/10.1016/j.dibe.2023.100292>.
- Mohammed, A., Burhan, L., Ghafor, K., Sarwar, W. and Mahmood, W. (2021a), “Artificial neural network (ANN), M5P-tree, and regression analyses to predict the early age compression strength of concrete modified with DBC-21 and VK-98 polymers”, *Neural Comput. Appl.*, **33**, 7851-7873. <https://doi.org/10.1007/s00521-020-05525-y>.
- Mohammed, A., Kurda, R., Armaghani, D.J. and Hasanipanah, M. (2021b), “Prediction of compressive strength of concrete modified with fly ash: Applications of neuro-swarm and neuro-imperialism models”, *Comput. Concrete*, **27**(5), 489-512. <https://doi.org/10.12989/cac.2021.27.5.489>.
- Nguyen, H., Vu, T., Vo, T.P. and Thai, H.T. (2021), “Efficient ML models for prediction of concrete strengths”, *Constr. Build. Mater.*, **266**, 120950. <https://doi.org/10.1016/j.conbuildmat.2020.120950>.
- Piro, N.S., Mohammed, A.S., Hamad, S.M., Kurda, R. and Qader, B.S. (2023), “Multifunctional computational models to predict the long-term compressive strength of concrete incorporated with waste steel slag”, *Struct. Concrete*, **24**(2), 2093-2112. <https://doi.org/10.1002/suco.202200023>.
- Prokhorenkova, L., Gusev, G., Vorobev, A., Dorogush, A.V. and Gulin, A. (2019), “CatBoost: unbiased boosting with categorical features”, *Advances in Neural Information Processing Systems 31 (NeurIPS 2018)*, Montréal, Canada, December.
- Qaidi, S., Yahia, A., Tayeh, B.A., Unis, H., Faraj, R. and Mohammed, A. (2022), “3D printed geopolymer composites: A review”, *Mater. Today Sustainab.*, **20**, 100240. <https://doi.org/10.1016/j.mtsust.2022.100240>.
- Rumelhart, D.E., Hinton, G.E. and Williams, R.J. (1986), “Learning representations by back-propagating errors”, *Nature*, **323**, 533-536. <https://doi.org/10.1038/323533a0>.
- Samaniego, E., Anitescu, C., Goswami, S., Nguyen-Thanh, V.M., Guo, H., Hamdia, K., Zhuang, X. and Rabczuk, T. (2020), “An energy approach to the solution of partial differential equations in computational mechanics via machine learning: Concepts, implementation and applications”, *Comput. Method. Appl. Mech. Eng.*, **362**, 112790. <https://doi.org/10.1016/j.cma.2019.112790>.
- Sergis, V. and Ouellet-Plamondon, C.M. (2022), “D-optimal design of experiments applied to 3D high-performance concrete printing mix design”, *Mater. Des.*, **218**, 110681. <https://doi.org/10.1016/j.matdes.2022.110681>.
- Shishegaran, A., Varace, H., Rabczuk, T. and Shishegaran, G. (2021), “High correlated variables creator machine: Prediction

- of the compressive strength of concrete”, *Comput. Struct.*, **247**, 106479. <https://doi.org/10.1016/j.compstruc.2021.106479>.
- Sun, B., Zeng, Q., Wang, D. and Zhao, W. (2022), “Sustainable 3D printed mortar with CO₂ pretreated recycled fine aggregates”, *Cement Concrete Compos.*, **134**, 104800. <https://doi.org/10.1016/j.cemconcomp.2022.104800>.
- Sun, Z.P., Sun, Y.S., Pang, M., Zhao, Y.H., Xu, Y.M., Li, H.H. and Xu, Y.L. (2021), “Research on ultra-high performance concrete suitable for 3D printing construction”, *New Build. Mater.*, **48**, 1-5.
- Wang, B. (2019a), “Anisotropy study on mechanics of 3D printed fiber-reinforced ceramsite concrete”, Master’s Degree Thesis, Hebei University of Technology, Tianjin, China.
- Wang, C., Song, L., Yuan, Z. and Fan, J. (2023), “State-of-the-art ai-based computational analysis in civil engineering”, *J. Industr. Informat. Integr.*, **33**, 100470. <https://doi.org/10.1016/j.jii.2023.100470>.
- Wang, Q. (2019b), “Research on optimal design and performance of 3D printed concrete”, Master’s Degree Thesis, Nanjing University of Science and Technology, Nanjing, China.
- Wang, Q. and Gao, C. (2019), “Application of PVA fiber in 3D printed concrete”, *Low Temp. Build. Tech.*, **41**, 3-6. <https://doi.org/10.13905/j.cnki.dwjz.2019.04.002>.
- Wang, S. (2022), “Preparation and research of 3D printing rubber powder cement-based materials”, Master’s Degree Thesis, Zhengzhou University, Henan, China.
- Wei, S.J. (2022), “Research on the preparation and mechanical properties of extrusion curing 3D printing concrete materials”, Master’s Degree Thesis, Harbin University of Science and Technology, Heilongjiang, China.
- Wu, T. (2021), “Research on the preparation and application of high-performance 3D printed concrete”, Master’s Degree Thesis, Southwest University of Science and Technology, Sichuan, China.
- Xu, H. (2022), “Research on 3D printed concrete based on recycled fine aggregate”, Master’s Degree Thesis, Shaoxing University of Arts and Sciences, Zhejiang, China.
- Young, B.A., Hall, A., Pilon, L., Gupta, P. and Sant, G. (2019), “Can the compressive strength of concrete be estimated from knowledge of the mixture proportions?: New insights from statistical analysis and ML methods”, *Cement Concrete Res.*, **115**, 379-388. <https://doi.org/10.1016/j.cemconres.2018.09.006>.
- Yu, Y., Li, B., Xu, L., Deng, Y.X., Ma, Q.N. and Xie, Y.F. (2021), “Effect of basalt fiber on the properties of 3D printing recycled cement-based materials”, *Concrete Cement Prod.*, **2021**, 45-49. <https://doi.org/10.19761/j.1000-4637.2021.12.045.05>.
- Zhang, L., He, D., Xu, W., Zhao, Q. and Teng, S. (2022), “Compressive strength prediction model of lightweight high-strength concrete”, *Mag. Civil Eng.*, **115**, 11512. <https://doi.org/10.34910/MCE.115.12>.
- Zhang, N., Lin, X.Q., Huo, L., Lu, L. and Zhang, T. (2021), “Effect of water-glue ratio on extrusion and mechanical properties of 3D printed concrete”, *China Build. Mater. Sci. Technol.*, **2021**, 30.
- Zhu, Y.M., Zhang, Y. and Jiang, Z.W. (2021), “Effect of hydroxypropyl methylcellulose on the properties of 3D printing mortar”, *J. Build. Mater.*, **24**, 1123-1130.